Nanoscale
Horizons

ROYAL SOCIETY
OF CHEMISTRY

COMMUNICATION

View Article Online
View Journal | View Issue

Check for updates

Cite this: *Nanoscale Horiz.*, 2025, **10**, 2080

Received 14th April 2025,
Accepted 25th June 2025

DOI: 10.1039/d5nh00241a

rsc.li/nanoscale-horizons

Conformation driven conductance modulation in single-stranded RNA (ssRNA)†

Arpan De, *[a] Arindam K. Das [b] and M. P. Anantram [a]

The structural attributes of RNA, especially co-transcriptional folding, have enabled RNA origami to construct complex 3D architectures, serving as a platform to build RNA-based nanodevices. However, the potential of RNA in molecular electronics is largely unexplored, mainly due to its inherent conformational fluctuations. Although this variability poses challenges for a precise understanding of the conductance properties of RNA, it also offers opportunities for tuning RNA-based molecular devices by exploiting their dynamic nature. Accordingly, our objectives in this paper are two-fold: (i) how do conformational fluctuations impact the charge transport properties of single stranded RNA (ssRNA), and (ii) how can these fluctuations be controlled? Toward that end, we first established a benchmark for ssRNA instability compared to double stranded RNA (dsRNA) based on molecular dynamics. Subsequently, we explore quantum transport across 123 distinct conformations, which show that the average conductance of ssRNA is 1.7 × 10^{-3} G_0, but with a high standard deviation of around 5.2 × 10^{-3} G_0. We demonstrate that the conductance of ssRNA is influenced primarily by backbone bending and nucleotide positioning. Specifically, while backbone bending tends to result in higher conductance at reduced end-to-end phosphorus distances, nucleotide positioning introduces significant stochasticity. To mitigate this variability, we also demonstrate that increasing the salt concentration can stabilize ssRNA, presenting a viable strategy for minimizing conductance fluctuations. Our findings reveal that if ssRNA conductance can be switched between folded and unfolded states, it can offer two distinct conductance modes. We anticipate the programmability of ssRNA folding and durability, coupled with its conductivity, can be leveraged for advancing molecular electronics.

New concepts

Advancement in molecular electronics relies on a precise understanding of charge transport at the nanoscale level. While DNA has been highly explored as a *syn*-biological electronic material, RNA remains largely unexplored despite its versatility in nanotechnology. This work provides the first comprehensive analysis of inherent conformation-driven conductance stochasticity in single-stranded RNA (ssRNA). We demonstrate that ssRNA conductance states are highly sensitive to conformational changes, particularly backbone bending and nucleotide arrangement. Importantly, we show that these conformational fluctuations can be regulated through environmental conditions such as salt concentration, offering a practical approach to control conductance variability. Our findings suggest that ssRNA programmable folding capability, combined with its variable conductance states, could enable the development of novel molecular switches and memory devices.

Introduction

The folding and unfolding of RNA transform a simple nucleotide chain into versatile 3D molecular complexes, playing a pivotal role in numerous biological functions.[1–4] For instance, RNA catalyzes peptide bond formation,[5] regulates translation,[6] assists in replication, and supports both protein synthesis[7] and viral propagation.[8] This intricate involvement of RNA complexes in modulating critical biological processes has motivated researchers to investigate its structural attributes for decades. Since 1999, a major research thrust has been prediction of secondary and tertiary structures of RNA sequences. Recently, Zhang *et al.* have provided a comprehensive review of state-of-the-art experimental and computational techniques for predicting RNA folding patterns.[9] Other excellent discussions on different methods used to solve RNA folding problems can be found in Seetin *et al.*[10] and Gardener *et al.*[11] From these studies, it can be inferred that secondary structures are largely governed by Watson–Crick (WC) and wobble base pairing, but transitions to tertiary structures are more complicated. Although these computational studies shed light on the folding patterns of RNA, they do not provide any insight into the underlying charge transport properties, which is crucial for

---

[a] *Department of Electrical and Computer Engineering, University of Washington, Seattle, WA 98195, USA. E-mail: arpan99@uw.edu*
[b] *Department of Computer Science and Electrical Engineering, Eastern Washington University, Cheney, WA, 99004, USA*

† Electronic supplementary information (ESI) available. See DOI: **https://doi.org/10.1039/d5nh00241a**

the design of next-generation nanotechnology. In this article, we aim to evaluate the impact of folding on RNA charge transport to assess the performance of RNA-based nano-devices.

RNA origami has emerged as a promising method for creating nanostructures through co-transcriptional folding of RNAs.[12] It enables the design of multitudes of complex RNA architectures for applications in medicine and synthetic biology. In 2018, Hoiberg *et al.* created an RNA octahedron *via* RNA origami for gene knockdown in cells.[13] Additionally, Krissanaprasit *et al.* utilized scaffold RNAs to bind thrombin, thereby improving anticoagulant activities.[14] Furthermore, Nguyen *et al.* demonstrated the regulation of gene expression with protein-binding RNA scaffolds.[15] A pioneering study by Han *et al.* successfully constructed diverse multikilobase single-stranded (ss) nanostructures including a 6337-nt RNA.[16] This study highlighted that self-folding of ssRNA can enable building of complex nanostructures without knots. Following up, Vallina *et al.* developed a multi-functional RNA origami robot, Traptamer, that can mechanically trap a fluorescent aptamer, reversibly control its fluorescence, and operate as a logic gate.[17] These studies elucidate the good programmability of single-stranded RNA scaffolds. The structural advantages of ssRNAs hold great potential for applications beyond biology, for example in building electronic devices. To advance this, it is essential to understand the underlying charge transport properties of RNA. Unlike DNA, RNA charge transport has not been explored extensively. Single-molecule conductance measurements have revealed that RNAs exhibit comparable, if not higher, conductance than DNAs.[18–20] Recently, Chandra *et al.* reported the conductance of single- and double-stranded RNAs to be around $0.001G_0$, where G_0 is the quantum of conductance.[21] However, conductance in RNA is characterized by high variability, which can be attributed to factors such as conformational changes and environmental conditions.[20] This fluctuation creates challenges but also opens possibilities for optimizing RNA-based molecular devices by harnessing their natural flexibility.

In this manuscript, we have focused on unraveling the implications of structural fluctuations on short single-stranded RNA (ssRNA) conductance through rigorous charge transport analysis. First, we present a comparative statistical analysis of structural variability between single- and double-stranded RNA with molecular dynamic simulations in Fig. 1. Second, we perform charge transport calculations on 123 conformations with different backbone and nucleotide configurations, and these results are illustrated in Fig. 2–5. Finally, we show how increasing the salt concentration can effectively harness the conformational fluctuations of ssRNA in Fig. 6, offering a viable solution for realizing RNA-based electronics.

Molecular dynamics results: ssRNA *vs.* dsRNA

We have selected the 10-base ssRNA sequence 5′-GGGGGCGGGG-3′ (5′-G_5CG_4-3′) to investigate conductance variability induced by folding and unfolding phenomena. For reference, we have also considered a 10-base pair dsRNA structure comprising the complementary sequence of the ssRNA, 5′-G_5CG_4-3′/3′-C_5GC_4-5′. Molecular dynamics (MD) simulations were conducted for 200 ns on both structures (details in Methods), with frames captured every 2 ps, yielding a total of 100 000 conformations. A comparative evaluation of the structural stability of ssRNA and dsRNA is presented in Fig. 1. The root mean square deviations (1D-RMSD), calculated relative to the initial frame, are shown in Fig. 1(a), where it is evident that dsRNA exhibits greater structural stability than ssRNA, with an average RMSD of 1.95 ± 0.52 Å, compared to 5.60 ± 1.15 Å for ssRNA. This trend is further corroborated by the 2D-RMSD plots shown in Fig. 1(b).

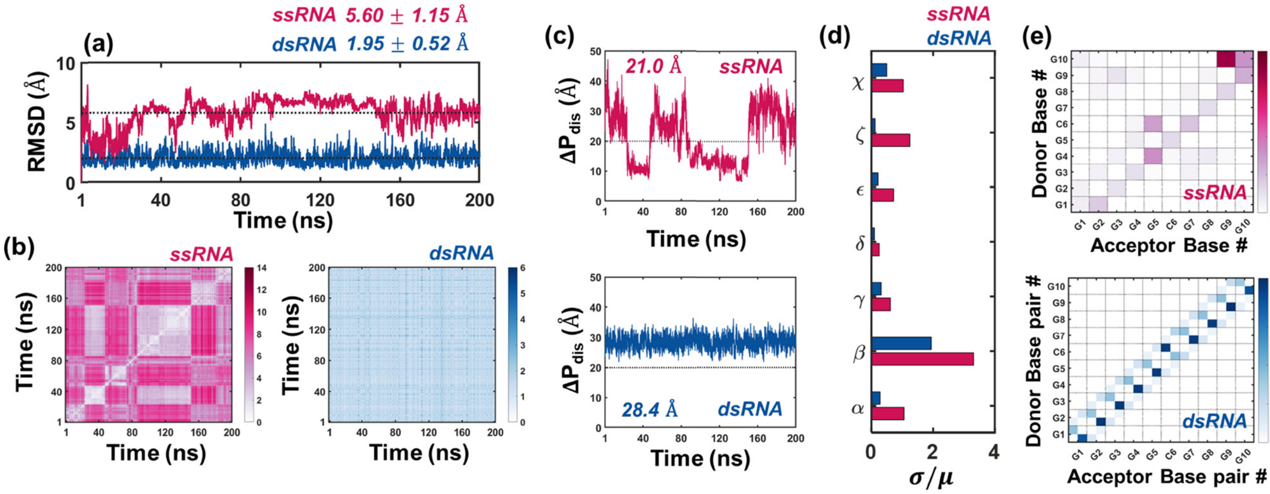

Fig. 1 Molecular dynamics results: ssRNA *vs.* dsRNA. (a) 1D RMSD *vs.* time; dotted black lines indicate the mean RMSDs. (b) 2D RMSD *vs.* time. (c) End-to-end phosphorus distances *vs.* time. (d) Coefficient of variation (σ/μ) for the seven backbone dihedral angles. (e) Hydrogen bond heatmaps between bases of ssRNA/base-pairs of dsRNA. In (c), the dotted lines are drawn to show that ssRNA mostly fluctuates between folded and unfolded configurations, while dsRNA is comparatively stable. In (e), the color bars (in units of Å) represent average hydrogen bonds over 100 000 conformations. An enlarged version of the heatmaps with corresponding average H-bond numbers are provided in Fig. S5(i) and (ii) (ESI†) for ssRNA and dsRNA respectively.

While 1D RMSD provides a reasonable estimate for structural stability, the 2D-RMSD heatmaps highlight the presence/absence of multiple low RMSD regions or stable conformation states. For ssRNA (Fig. 1(b), left), we identify six distinct patches of low RMSD (<5 Å). Among these, the biggest patch is approximately between 85–150 ns. On the contrary, the 2D-RMSD heatmap of dsRNA (Fig. 1(b), right) has a maximum value of 5.75 Å, significantly lower than the 13.32 Å observed for ssRNA. This results in the absence of low RMSD "patches" in dsRNA, underscoring its "stability throughout the MD trajectory." To gain deeper insight into the conformational dynamics of both ssRNA and dsRNA, we employed the end-to-end phosphorus distance (ΔP_{dis}), defined as the distance between 1st and 9th phosphorus atoms, as a key metric for analysis. The value of ΔP_{dis} is directly proportional to the bending of the backbone. From Fig. 1(c), we observe that in the case of ssRNA, ΔP_{dis} varies considerably (unlike dsRNA, shown in the bottom panel of Fig. 1(c)), spanning a range from 6.40 to 47.18 Å, with an average value of 21 Å. We used this average value to classify the conformations into folded ($\Delta P_{\text{dis}} < 21$ Å) and unfolded ($\Delta P_{\text{dis}} \geq 21$ Å) states, yielding a folding probability of 47.88% (*i.e.*, 47 880 out of 100 000 conformations have $\Delta P_{\text{dis}} < 21$ Å). When correlating ΔP_{dis} values with low RMSD patches in the 2D-RMSD heatmap, we observe that the ssRNA sequence exhibits stable configurations in both folded and unfolded states. For instance, for the low RMSD patches between ≈20–40 ns and ≈85–150 ns in (Fig. 1(b), left), the ssRNA sequence has a ΔP_{dis} value of less than 21 Å. For other low RMSD patches, ΔP_{dis} is relatively higher, suggesting shuffling between the folded and unfolded states. In contrast, dsRNA exhibits a tighter distribution of ΔP_{dis} (see Fig. 1(c), bottom), ranging from 21.72 to 36.48 Å with a mean value of 28.4 Å which is consistent with the trends in RMSD plots in Fig. 1(a) and (b). Note that for dsRNA, we obtained two distributions of ΔP_{dis} for 5′-3′ and 3′-5′ strands, which are very similar to each other (see Fig. S1, ESI†); in (Fig. 1(c), bottom), we show the mean ΔP_{dis} over both strands. We also analyzed the distributions of the seven backbone dihedral angles to further characterize the structural fluctuations of ssRNA and dsRNA, as shown in Fig. 1(d). It is evident that the coefficients of variation (CV) of all dihedral angles, derived from 100 000 conformations, are considerably higher for ssRNA than dsRNA, which is consistent with our observations regarding RMSDs and ΔP_{dis} values shown in Fig. 1(a)–(c). In particular, the CV of the dihedral angle between bases and backbone (χ) for ssRNA is 51.6% higher compared to dsRNA.

To further probe the backbone dihedral distributions, we have presented the residue-wise time evolutions of backbone dihedrals for ssRNA and dsRNA in Fig. S2 and S3 (ESI†) respectively. For dsRNA, the dihedrals are extremely stable with minimal fluctuations (Fig. S3, ESI†), consistent with the 2D RMSD heatmap in Fig. 1(b). In contrast, ssRNA demonstrates pronounced fluctuations in its backbone dihedrals (Fig. S2, ESI†). Specifically, the 3′-end residues' dihedrals (primarily α, δ, ζ) show significant perturbation between ≈20–200 ns. We also observe minor variations in the interior residue dihedrals from ≈ 80 ns, coinciding with the onset of ssRNA folding ($\Delta P_{\text{dis}} <$ 21 Å, Fig. 1(c), top). We attribute these dihedrals' perturbations of the interior bases to the folding of the structure, which we hypothesize is triggered by fluttering of the 3′-end residues. A comparative analysis of probability densities for all dihedral angles is depicted in Fig. S4 (ESI†). In general, we observe that the pdf's of ssRNA are multimodal, in contrast to unimodal for dsRNA (with the exception of β). We also observe that while the locations of the primary peaks for ssRNA align closely with those for dsRNA, the secondary peaks for ssRNA can be attributed to folding-induced dihedral perturbations.

To further elucidate the underlying reasons for structural dynamics, we next examine hydrogen bonding between different residues. Considering each nucleotide as both a donor and an acceptor for hydrogen bonding, we have created heatmaps with the average number of hydrogen bonds, shown in Fig. 1(e), which highlights two distinct types of hydrogen bonds: (i) intra-nucleotide hydrogen bonds, formed between atoms in the backbone and base of the same nucleotide (represented by the main diagonal elements) and (ii) inter-nucleotide hydrogen bonds, formed between backbone and base of one nucleotide and those of another nucleotide. An enlarged versions of the heatmaps with corresponding average hydrogen bond numbers are provided in Fig. S5(i) and (ii) (ESI†) for ssRNA and dsRNA respectively. Inter-nucleotide hydrogen bonds can be further subdivided into two categories: bonds between adjacent nucleotides (depicted by elements on the upper and lower diagonals in Fig. 1(e)), and those between non-adjacent nucleotides (represented by all other elements except those on the main, sub, and super diagonals). The presence of hydrogen bonds between adjacent bases indicates stabilization of the ssRNA, while bonds between non-adjacent bases suggest a higher likelihood of folding. Intra-nucleotide hydrogen bonds occur only when the nucleotide comes close to the backbone during the MD trajectory. From Fig. 1(e), we can make three key observations. First, in the case of ssRNA (Fig. 1(e), top), a significant number of hydrogen bonds are observed between adjacent bases (elements on sub and super-diagonals) as well as non-adjacent bases, such as those between bases 9 & 3, 1 & 10, and 4 & 8. The former (latter) type of bonding explains the stability of the unfolded (folded) conformations, which has been explicitly demonstrated in Fig. S6 (ESI†). Second, intra-nucleotide hydrogen bonding is considerably higher for the terminal nucleotides (1 and 10), which can be attributed to the twisting of the nucleotide, bringing it in proximity to the backbone and allowing hydrogen bonds to form between the backbone and base. However, the occurrence of such twisting is less likely in the non-terminal bases, resulting in low hydrogen bonds along other diagonal elements in (Fig. 1(e), top). Finally, in dsRNA (Fig. 1(e), bottom), it is evident that hydrogen bonds within a base pair dominate those between adjacent base pairs. This explains the tight distribution of ΔP_{dis}dsRNA in (Fig. 1(c), bottom).

Conductance variations in ssRNA

In Fig. 1, we have established the structural instability associated with ssRNA. In this section, we undertake an analysis of

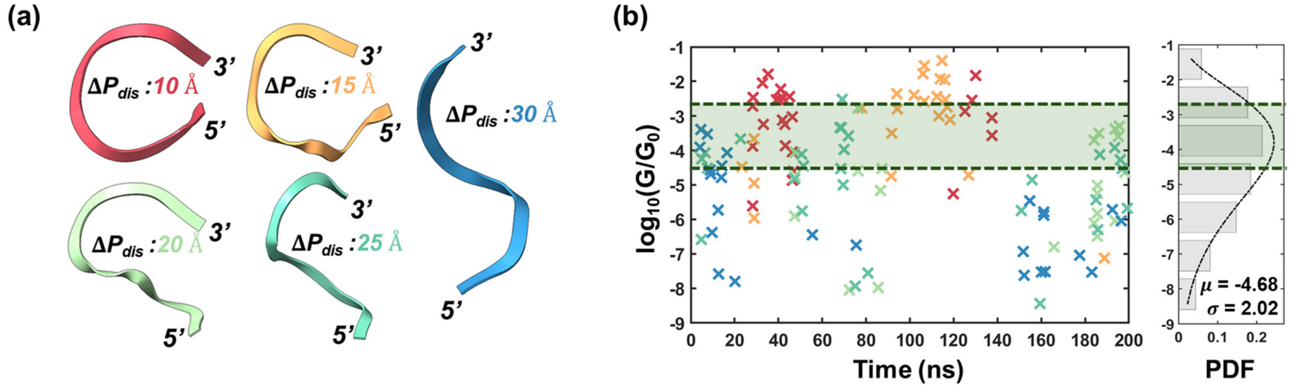

Fig. 2 Conductance stochasticity of ssRNA. (a) Representative backbone orientations of ssRNA for nominal ΔP_{dis} values 10, 15, 20, 25 & 30 Å. (b) Left: Conductance as a function of time. The markers (indicated by ×) are color-coordinated to panel (a). Right: Probability distribution of all the log of conductance values obtained from 123 conformations (bar plots). The dotted line is the fitted curve with gamma distribution (α = 5.3424, β = 0.8767). The green shaded regions enclosed within dotted envelopes represent the conductance dispersion limits of dsRNA of this work. The conductance values for dsRNA have been provided in Table S1 (ESI†).

the impact of structural instability on the conductance of ssRNA. Toward that end, we first classified the 100 000 ssRNA conformations into five distinct categories based on ΔP_{dis} values, namely, 10 Å to 30 Å in steps of 5 Å with a tolerance of 10% (the nominal ΔP_{dis} values for the five categories are 10, 15, 20, 25, and 30 Å). From each category, we have chosen frames based on the number of stacked bases, leading to a total of 123 selected conformations. The detailed frame selection methodologies for both ssRNA and dsRNA are provided in Methods.

Typical representations of the backbone orientations for the five ΔP_{dis} categories from 10 Å to 30 Å are shown in Fig. 2(a). We performed energy-dependent decoherence probe-based charge transport calculations (details available in Methods) on the selected structures with the contacts connected to the first and last bases. We then computed the zero-bias conductance of each selected conformation with the Fermi energy corresponding to the HOMO energy. These conductance values are shown as a function of time in (Fig. 2(b), left). To better illustrate the conductance dispersion, we have also shown the probability density function (PDF) in (Fig. 2(b), right). The mean and standard deviation of the pdf of $\log_{10}\left(\frac{G}{G_0}\right)$ are obtained to be −4.68 Å and 2.02 Årespectively, where G and G_0 are the ssRNA conductance and quantum of conductance respectively. The high standard deviation suggests that conductance variability is closely related to conformational fluctuations. The pronounced conductance stochasticity observed in ssRNA is attributed to its ability to exhibit multiple metastable states, unlike the well-characterized dsDNA, which generally remains unfolded and exhibits a narrow conductance distribution – as supported by the dsRNA conductance data presented in this study (see Table S1, ESI†).

Next, to explore the dependence of conductance dispersion on ΔP_{dis}, we have presented the conductance distributions of conformations for each category of ΔP_{dis} in Fig. S7 (ESI†). We observe that the average conductance decreases from folded (ΔP_{dis} = 10, 15 Å) to unfolded (ΔP_{dis} = 25, 30 Å) states. Overall, it can be inferred that folding, in general, leads to an increase in conductance along with lesser variability, a property which can be leveraged for next-generation synthetic-biology-based electronics.

Electronic properties of conformations

A striking observation across all categories in Fig. 2(b) is the substantial disparity between the maximum and minimum conductance values observed among the conformations. The corresponding extreme conductance values for all five ΔP_{dis} categories are summarized in Table 1. For every ΔP_{dis} category, the conductance spread (defined as the ratio of maximum to minimum conductance in a category) was found to range between $\approx 10^3$–10^6 G_0, which is substantial and highlights the significant influence of conformation in determining conductance. To unravel the impact of conformation on conductance, we have studied the extreme conductance cases, low conductance conformation (LCC) and high conductance conformation (HCC) of ΔP_{dis} = 15, 20, and 25 Å. For a holistic understanding of conductance fluctuations, we have compared the conformations based on four metrics.

First, we analyze the structural differences between LCCs/HCCs of each category in Fig. 3. For ΔP_{dis} = 15 Å, we notice that the distance between 3′ and 5′ ends is lower for HCC in contrast to LCC (see Fig. 3(a)). Quantitatively, the distance between the center of masses of terminal bases 1 and 10 is 10.13 Å (8.41) for LCC (HCC). This distinction becomes more pronounced for

Table 1 Summary of lowest and highest conductance values for the five categories of ΔP_{dis}

G/G_0	ΔP_{dis}: 10 Å	ΔP_{dis}: 15 Å	ΔP_{dis}: 20 Å	ΔP_{dis}: 25 Å	ΔP_{dis}: 30 Å
LCC	2.48×10^{-6}	7.51×10^{-8}	8.91×10^{-9}	3.63×10^{-9}	1.58×10^{-8}
HCC	1.62×10^{-2}	4.00×10^{-2}	1.70×10^{-3}	3.00×10^{-3}	4.12×10^{-4}
Ratio	$\mathbf{6.53 \times 10^{3}}$	$\mathbf{5.33 \times 10^{5}}$	$\mathbf{1.91 \times 10^{5}}$	$\mathbf{8.26 \times 10^{5}}$	$\mathbf{2.61 \times 10^{4}}$

LCC: lowest conductance conformation; HCC: highest conductance conformation; G_0: quantum conductance

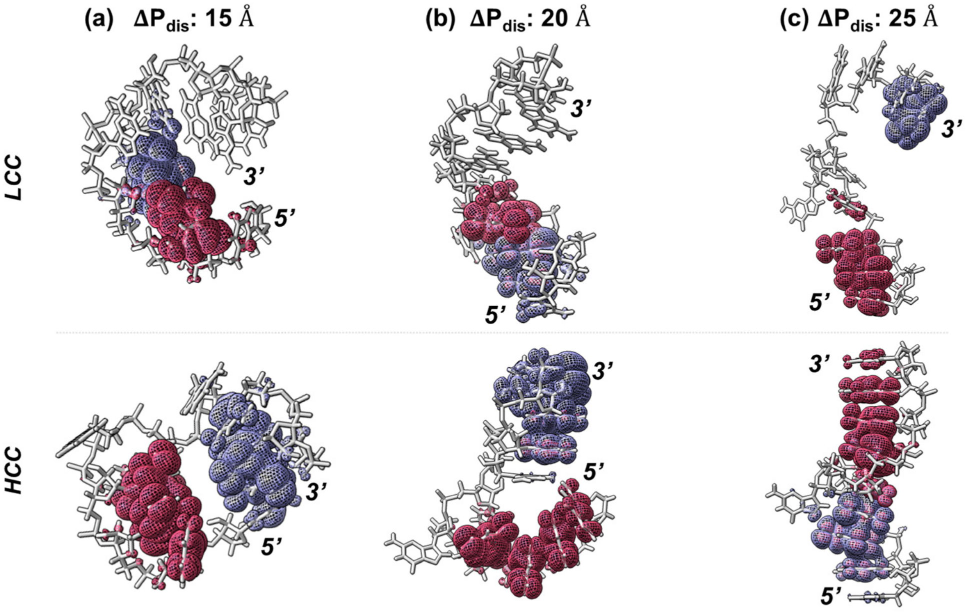

Fig. 3 Wavefunction distribution. Configuration of the lowest and highest conductance configurations (LCC and HCC respectively) for three categories of end-to-end phosphorus distances, ΔP_{dis}: (a) 15 Å, (b) 20 Å, and (c) 25 Å with orbital maps of corresponding HOMO (purple) and HOMO−1 (pink) energy level. Wavefunctions with absolute value greater than or equal to 0.005 are shown.

ΔP_{dis} = 20 Å (Fig. 3(b)), where the separation between the terminal bases is 23.02 Å for LCC *vs.* 13.31 Å for HCC. Moreover, unlike the LCC structure, the 5′ end in HCC is close to the 7th and 8th bases (6.68 Å and 7.65 Å respectively). A similar trend can be noticed for ΔP_{dis} = 25 Å (Fig. 3(c)). In this case, the distances between the terminal bases are 28.63 Å and 24.87 Å for LCC and HCC respectively. These results, combined with the conductance data provided in Table 1, suggest that the distance between terminal bases and conductance should be correlated. Intuitively, this is justified since a lower terminal base distance decreases the hopping length, leading to higher conductance.

However, the inter-terminal base distance alone cannot completely account for the substantial conductance ratio between LCCs and HCCs. To further address this issue, we have considered a second metric, delocalization of HOMO and HOMO−1 orbitals among the bases. A higher delocalization suggests better orbital overlapping between the bases, which in turn is indicative of better charge transport. For the three specific cases depicted in Fig. 3, we find that the proximity of bases plays a crucial role in orbital delocalization, for both folded and unfolded configurations. For ΔP_{dis} = 15 Å, a closer observation reveals that the 1st base has moved closer to the 10th base in HCC, whereas in LCC it swings away. Consequently, the HOMO orbital is delocalized over bases 1, 7, 8, 9, 10 for HCC, while it is delocalized only over bases 3, 4, 5, 6 for LCC. The HOMO−1 orbital is also delocalized for HCC, but over bases 2, 3, 4, 5, whereas for LCC, it remains delocalized on bases 2, 3, 4. Similarly, for ΔP_{dis} = 25 Å, we observe a delocalization over bases 1 to 8 for HCC. In contrast, the proximity of 3′ terminal bases (8, 9, 10) for LCC leads to strong orbital overlap, causing the HOMO orbital to localize near the 3′ terminal. The trends of high delocalization for HCC become more evident for the HOMO−1 orbital.

Interestingly, for ΔP_{dis} = 20 Å, although the inter-base distances are lower in HCC than LCC (Fig. 3(b)), the HOMO orbital delocalization is more pronounced for LCC (over bases 1, 2, 3, 4, 5) than HCC (over bases 8, 9, 10). However, we find that the HOMO−1 orbital is more delocalized for HCC than LCC. To quantify orbital localization, we have computed the inverse participation ratio ($\text{IPR} = \sum_i |\Psi_i|^4 \Big/ \left(\sum_i |\Psi_i|^2\right)^2$, where $|\Psi_i|^2$ is the probability of finding an electron at the *i*th residue).[22] The greater the value of IPR (maximum value is 1), the greater is the orbital localization. Table 2 summarizes the IPR values and energy levels for the first three HOMO energy levels for ΔP_{dis} = 15, 20, 25 Å. The corresponding probabilities ($|\Psi_i|^2$) are shown in Fig. S8 (ESI†). We observe from Table 2 that the IPR values of LCC and HCC at corresponding HOMO (HOMO−1) energies are 0.85 (1.00) and 1.00 (0.72) for ΔP_{dis} = 20 Å. Additionally, the HOMO & HOMO−1 levels differ by 150 meV ($\approx 5k_{\text{B}}T$) and 20 meV ($< \approx k_{\text{B}}T$) respectively for LCC and HCC. This suggests that when the Fermi energy is near the HOMO level for HCC, both HOMO and HOMO−1 orbitals can participate in electronic transport due to their relatively small energy separation. Therefore, we can conclude that for the ΔP_{dis} = 20 Å category, small energy differences between the first few HOMOs, coupled with strong orbital delocalization, results in higher conductance of HCC. The trend of energetically close HOMOs with lower IPR values for HCCs relative to LCCs is also applicable for the other two categories (ΔP_{dis} = 15 and 25 Å).

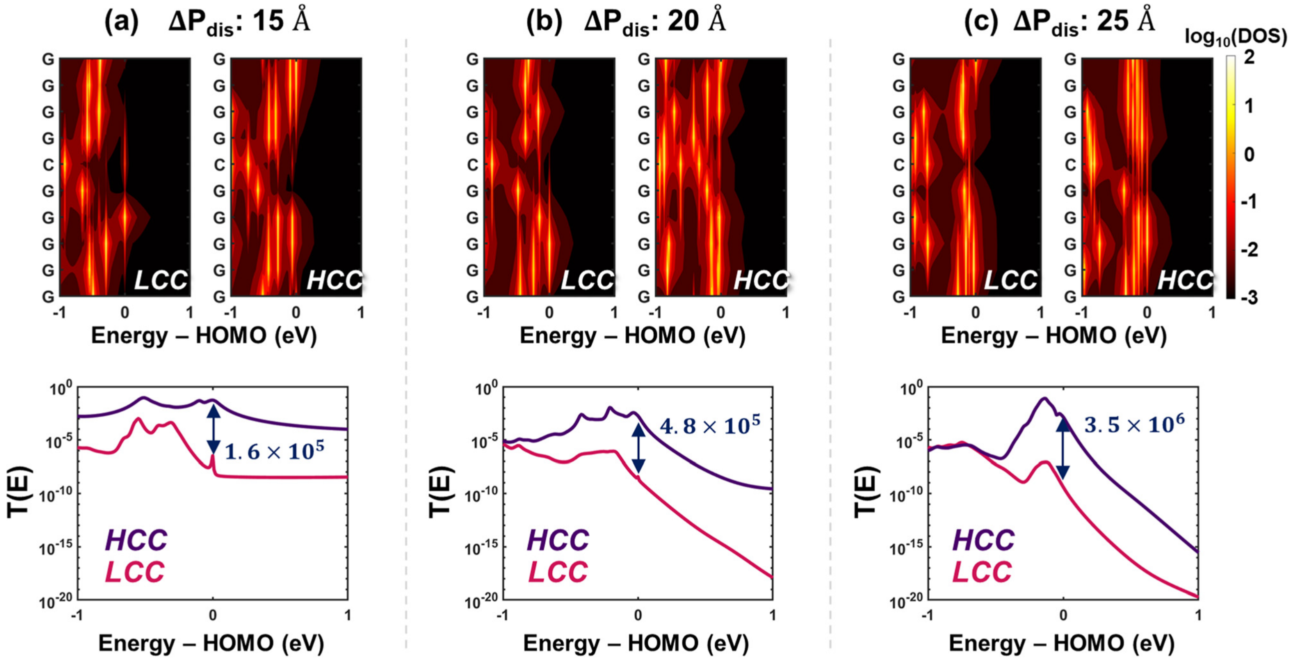

Fig. 4 Charge transport properties. Density of states and transmission profiles for HCCs and LCCs are shown for ΔP_{dis}: (a) 15 Å (b) 20 Å and (c) 25 Å. (Top row) Partial density of states (PDOS) for every residue site. The left and right panels show the PDOS distributions for LCC and HCC conformations respectively. (Bottom row) Transmission profiles as a function of energy. The ratios of transmission at HOMO energy level for HCC to LCC are also indicated.

From the preceding discussions, we make two key observations: (i) while higher delocalization is typically indicative of better charge transport, conductivity is ultimately governed by the intricate interplay between inter-base distances and the extent of orbital delocalization, and (ii) although conductance is calculated with the Fermi energy at the HOMO energy level, to fully comprehend the underlying electrostatics, it is essential to analyze the energy differences among the first few HOMO energies. This additional analysis provides a more complete picture of how orbital characteristics and their variations impact charge transport in ssRNA. Our observations also extend to ΔP_{dis} = 10 and 30 Å categories, as illustrated in Fig. S9 (ESI†).

Next, we have also analyzed the conductance trends based on density of states of the conformations. The 2D DOS heatmaps are shown in (Fig. 4, top row) and the partial DOS (PDOS) of each conformation at different energies are shown in Fig. S10–S14 (ESI†). We observe that the lower delocalization in HCC for ΔP_{dis} = 20 Å is also reflected in the base-wise PDOS (see Fig. 4(b)), causing the total DOS at HOMO of the LCC to be higher than that of the HCC. But as we move into the HOMO band, even a small shift of 10 meV results in the total DOS as well as base-wise partial DOS of HCC to surpass those for LCC (Fig. S15, ESI†). This explains the high conductance of the HCC. For the other two categories, ΔP_{dis} = 15 and 25 Å, the total DOS of HCCs at HOMO is substantially larger than corresponding LCCs, a trend that holds for other energies close to HOMO (see Fig. S11 and S13, ESI†). Additionally, we observe from the top row of Fig. 4 that for all ΔP_{dis} categories, high DOS patches are concentrated near or at HOMO for the HCC. These high DOS energy levels primarily contribute to charge transport, resulting in a high transmission probability for HCCs at HOMO energy level (Fig. 4, bottom row). From the transmission profiles across different ΔP_{dis}, we make two observations: (i) for both LCC and HCC, the transmission at HOMO energy drops with increase in ΔP_{dis},. This finding also holds for ΔP_{dis} = 10 and 30 Å. (ii) The transmission in the bandgap is considerably higher for folded (ΔP_{dis} = 10 and 15 Å) states in contrast to unfolded (ΔP_{dis} = 25 and 30 Å) states. At lower ΔP_{dis}, the tunneling probability between terminal bases is higher due to their proximity, while at higher ΔP_{dis}, transport is more dependent on hopping between bases. Given that tunneling between terminal bases serves as a promising transport mechanism, conformations in folded states result in higher transmission in the bandgap, despite having negligible DOS.

The conductance of ssRNA depends primarily on the efficiency of carrier transport between the two contacts, which are bases 1 and 10 in our simulation setup. The three charge transport properties we have discussed – inter-base distance, orbital delocalization, and density of states – individually highlight the underlying reasons for significantly higher conductance (see last row in Table 1) in HCC over LCC across all ΔP_{dis} categories. However, to comprehensively understand the rationale behind the high conductance ratio between HCC and LCC, we devised a fourth metric, *probable pathways*, comprising four components: (i) inter-base distance (ii) total DOS (iii) orbital overlap, and (iv) length of a path (number of nodes). To identify the most probable paths from base 1 to 10, we employed a graph network-based approach, which is explained in Methods. In this framework, individual bases are treated as nodes of a

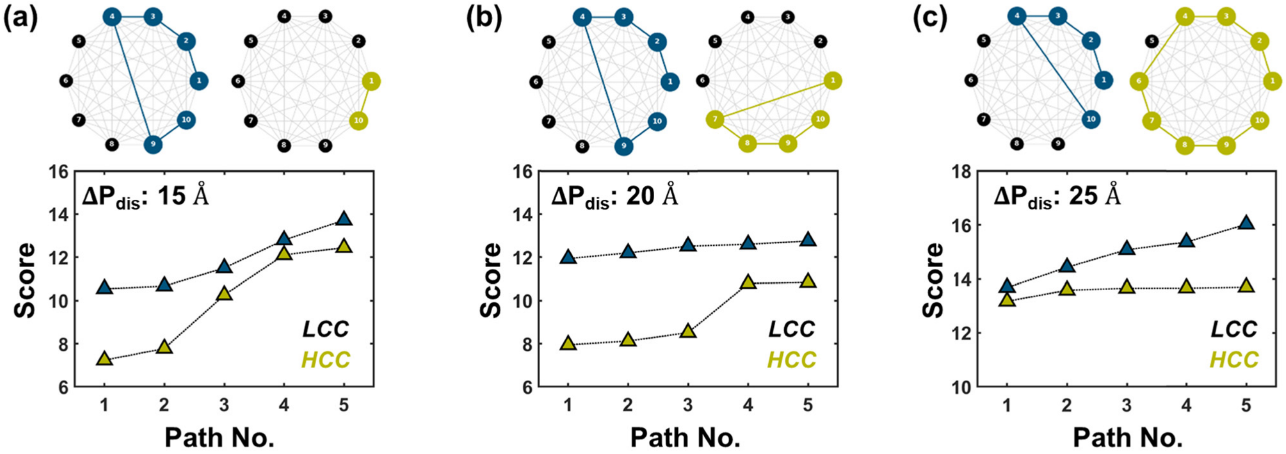

Fig. 5 Probable pathways. (Top row) The most probable (least cost) paths, indicated by colored nodes/edges, for HCCs and LCCs when ΔP_{dis} = 15, 20, and 25 Å. (Bottom row) The total cost ("score") of the top five probable paths.

graph and the cost of a path between two nodes is based on the aforementioned charge transport properties. The cost of a node is computed based on PDOS of the bases in a path while the cost of an edge is a function of distance and orbital overlapping between successive bases in that path. We have only considered simple paths (*i.e.*, no repeating nodes) for our analysis. A smaller path score represents more favorable pathways. The top row in Fig. 5 shows the most probable paths for HCCs and LCCs when ΔP_{dis} = 15, 20, and 25 Å and the bottom row shows the total cost ("score") of the top five probable paths. To validate the significance of the proposed pathways, we first compute the conductance at the HOMO level for each conformation by selectively disabling the hopping between bases involved in a specific path. We then calculate the conductance ratio by comparing the conductance of the fully connected system with that of the modified system where the hopping between bases in the chosen path is selectively turned off (see Fig. S16, ESI†). The most probable paths shown in the top row of Fig. 5 show a dramatic reduction in transmission at HOMO energy by $\approx 10^2$–10^8 times when the paths are disrupted, underscoring the significance of these paths in facilitating charge transport. From the bottom row of Fig. 5, it is evident that the scores of the top five paths for HCCs are considerably lower than those of LCCs, particularly for the ΔP_{dis} = 15 and 20 Å categories. Interestingly, when ΔP_{dis} = 15 Å, while the most probable (least cost) path for HCC is a direct hop between bases 1 and 10, that for LCC is rather circuitous ($1 \rightarrow 2 \rightarrow 3 \rightarrow 4 \rightarrow 9 \rightarrow 10$). The proximity of terminal bases in HCC allows for direct transport between the two contact bases, which is not possible in LCC due to the larger terminal base separation. We note that the most probable path agrees with the probability ($|\Psi|^2$) of HOMO orbital (see top five pathways along with their scores in Fig. S15, ESI†). We believe that direct transport reduces the probability of scattering, which explains the higher conductivity of HCC than LCC for ΔP_{dis} = 15 Å. For ΔP_{dis} = 20 Å, the most probable path for HCC ($1 \rightarrow 7 \rightarrow 8 \rightarrow 9 \rightarrow 10$) includes a hop from base 1 to 7, which can be attributed to the proximity of these bases as shown in Fig. 5(b). This arrangement facilitates better transport in HCC compared to LCC, despite the former having lower HOMO orbital delocalization. While inter-base distances, particularly terminal-base distances, play a pivotal role in enhancing conductance, the total DOS of bases involved in a pathway can also contribute significantly toward charge transport, especially for the unfolded conformational states. For instance, when ΔP_{dis} = 25 Å, the total DOS of all bases involved in the most probable path in HCC is considerably higher than LCC (Fig. S13, ESI†), despite the former having a longer route. A similar observation can be made for ΔP_{dis} = 30 Å category (Fig. S15, ESI†). This demonstrates that while the length of the transport pathway (as measured by number of hops) is a factor, the higher DOS in HCC compensates for the longer route by enabling more efficient transport.

Harnessing conformational fluctuations of ssRNA

From an applications perspective, the high stochasticity in ssRNA conductance observed in Fig. 2 is undesirable. As demonstrated previously, the underlying reason for this variability is structural instability. Taking a cue from previous studies which have shown that salt concentration plays a vital role in stabilizing RNA conformations,[23–26] we considered low (~100 mM with 11 Cl^- ions) and high (~450 mM with 41 Cl^- ions) salt concentrations in our calculations, as illustrated in Fig. 6. Initially, we validated our setup by computing the radial distribution functions (RDF) for Na^+ ions relative to the phosphate group in ssRNA, as well as water molecules around Na^+ ions (hydration shell). The computed RDFs agree with H. Knechtel *et al.* within a tolerance of 2–15%, as demonstrated in Fig. S17 (ESI†).[23] The computed RDFs also match very closely with Stefan *et al.* (2.35 Å)[27] The 1D-RMSD in Fig. 6(a) clearly demonstrates that the average RMSD decreases with an increase in salt concentration. Comparing the 2D RMSD heatmaps in (Fig. 6(b) with Fig. 1(b), left), we observe that

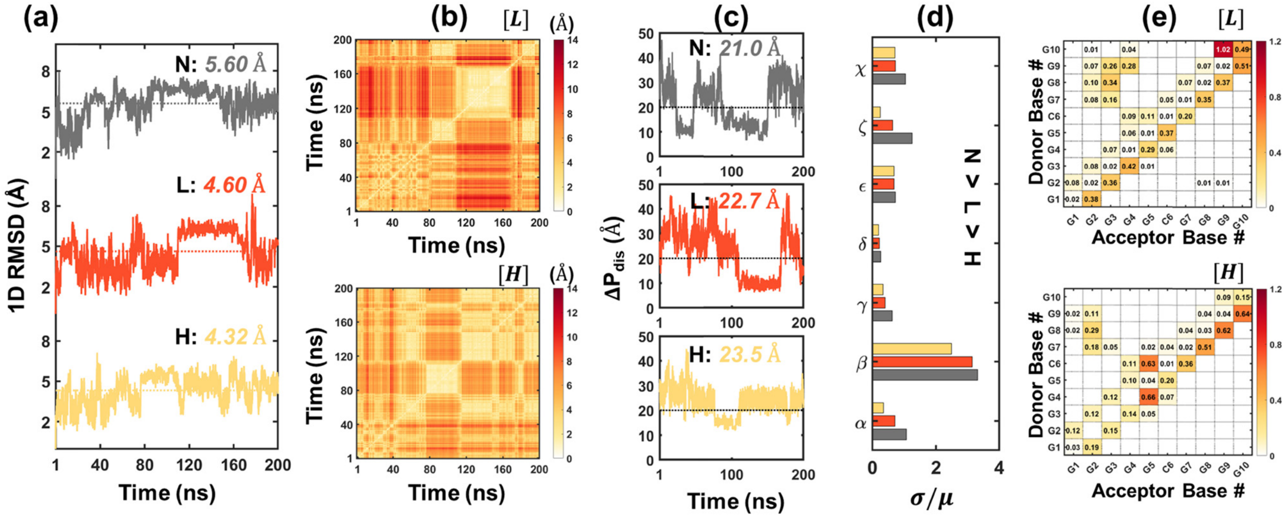

Fig. 6 Impact of salt concentration. (a) 1D-RMSD results for (top panel) negligible, N (middle panel) low, L and (bottom panel) high, H salt concentrations. The dotted lines represent the average RMSD. (b) 2D RMSD heatmaps showing higher salt concentration leads to overall lower RMSD. (c) End-to-end phosphorus distances. The dotted lines represent the average ΔP_{dis}. (d) Coefficient of variation (σ/μ) for negligible (yellow), low (orange), and high (grey) salt concentrations. (e) Hydrogen bond heatmaps for (top panel) low and (bottom panel) high salt concentrations. Color bars in (e) represent average hydrogen bonds over 100 000 conformations. Fewer number of hydrogen bonds between non-adjacent bases suggest a reduced folding tendency. The numbers on each grid have been rounded off to one place after decimal and nearest integer.

increasing the salt concentration leads to a reduction in overall structural fluctuations during the MD trajectory. This is evident from the increase in low RMSD patches as the salt concentration rises. In Fig. 6(c), we plot ΔP_{dis} as a function of time for three different salt concentrations: (i) negligible (N, $\text{Cl}^- = 0$), (ii) low (L, $\text{Cl}^- = 11$), and (iii) high (H, $\text{Cl}^- = 41$). Indeed, the folding of ssRNA, as quantified by ΔP_{dis}, has dropped from 47.88% in the "no salt" case to 36.89% and 23.44% for low and high salt concentrations respectively. The backbone structural stability is also reflected in a decreasing trend of the coefficient of variation (CV) of the six backbone dihedrals (α, β, γ, δ, ε, ζ) with increasing salt concentration (Fig. 6(d)). A lower CV of the dihedral angle χ, which signifies fluctuations of nitrogenous bases, attests to low conductance stochasticity. Finally, the hydrogen bonding analysis in Fig. 6(e) reveals the presence (absence) of more hydrogen bonds between adjacent (non-adjacent) bases at higher salt levels, explaining the increased stability of the ssRNA conformation. These observations suggest that increasing salt concentrations can be a viable approach to controlling structural fluctuations in ssRNA. This stabilization, in turn, reduces the variability in conductance, offering a more consistent performance. Such control over conductance spread could be strategically leveraged to develop ssRNA-based electronic devices, where reliable charge transport is critical for functionality.

Discussion

In this study, we have systematically explored the charge transport properties of a short (10-base) single-stranded RNA (ssRNA), which is desirable for electronic applications. Although our analysis focuses on a specific ssRNA sequence, we anticipate that our findings should extend to any short ssRNA. We started by comparing the structural stability of single- and double-stranded RNAs (Fig. 1). The comparison was made using three key metrics: 1D and 2D RMSDs, end-to-end phosphorus distance (ΔP_{dis}) and backbone dihedral angles. Our analysis revealed that while dsRNA exhibits greater stability in all three aspects, ssRNA is characterized by large conformational fluctuations. The superior stability of dsRNA can be attributed to the presence of intra-base pair hydrogen bonding which is absent in ssRNA (Fig. 1(e)). Moreover, our hydrogen bonding heatmaps depict that ssRNA is stabilized primarily by hydrogen bonds between adjacent/non-adjacent bases in an unfolded/folded state. This suggests that in short ssRNA sequences, hydrogen bonding between adjacent bases plays a critical role in determining the folding probabilities, offering a potential design rule for manipulating ssRNA structures. Next, using an MD-frame selection procedure based on stacked bases and ΔP_{dis}, we selected 123 frames from the pool of 100 000 conformations to perform charge transport calculations (Fig. 2). We note that although state-of-the-art sampling methods (*e.g.*, umbrella sampling, metadynamics, and adaptive sampling) exist which aim to achieve adequate conformational sampling while minimizing the computational cost, our frame selection procedure proved adequate to capture conformations with a wide conductance spread. S. Chandra *et al.* performed STM-BJ-based conductance measurements of dsRNA and DNA:RNA hybrid, each 11 bp long with a poly-GC sequence and reported a conductance of $\approx 1.63 \times 10^{-3} G_0$.[20] More recently, S. Chandra *et al.* have also reported the conductance of 5-mer and 10-mer ssRNA to be ≈ 2.9– $3.6 \times 10^{-3} G_0$.[21] Table S2 compares the single-molecule conductances of this work to the previously reported studies. Comparing the pdf in (Fig. 2(b), right) to the previously reported conductance data, we observe that the experimental conductance values are within one standard deviation of our mean computational conductance. The higher standard deviation in our work is due to our consideration of diverse configurations, which are likely non-existent in the break-junction experiments. The main goal of our study is to highlight the impact of conformational fluctuations on ssRNA conductance. This necessitates sampling a broad range of configurations. We anticipate that future experimental studies will reveal the broad range of conductance values including the high conductance states, as predicted in this work.

The significant spread of the conductance spectrum points towards the strong influence of conformational fluctuations on ssRNA charge transport. While conductance tends to increase with lower ΔP_{dis}, the wide spread of conductances across all ΔP_{dis} categories underscores the importance of nucleotide positioning. To probe the cause of drastic conductance disparities between two conformations with similar ΔP_{dis}, we conducted a detailed quantum mechanical analysis on the extreme conductance conformations and observed a strong connection between the inverse participation ratio (IPR) for first few HOMOs and conductance (Fig. 3 and Table 2). Moreover, we established that the energy differences among first few HOMOs is considerably lower in high conductance conformations (HCC) over low conductance (LCC) ones (Table 2). For HCCs, with Fermi energy at HOMO level, multiple HOMO energies can partake in electronic transport. However, in certain conformations, such as when $\Delta P_{\mathrm{dis}} = 20$ Å, inter-base distance dominates other electronic properties in determining ssRNA conductivity since shorter hopping distances facilitate more efficient carrier transfer between bases. This observation is corroborated by the transmission profiles shown in Fig. 4 (bottom). A higher transmission probability in the bandgap for a folded configuration suggests that the transport mechanism is dominated by direct tunneling between terminal bases. With no prospect of such tunneling in an unfolded state, transmission drops significantly. These observations suggest that while ΔP_{dis} is a global factor which influences ssRNA conductance, inter-base distances enable local modulation of charge transport. To substantiate this hypothesis, we proposed a probable pathways metric for carrier transport based on path length, electronic properties, and inter-base distances. These pathways can offer valuable insight into the mechanisms which induce differences in conductance among conformations. Efficient charge transport favors shorter hopping distances and higher availability of states in the hopping sites. We observed that while pathways in folded structures are governed largely by inter-base distances, those in unfolded structures depend on orbital delocalization and density of states. Finally, we explored practical approaches to harness ssRNA structural fluctuations and reduce conductance stochasticity. In Fig. 6, we demonstrated that higher salt concentrations stabilize ssRNA, as reflected in multiple structural attributes.

Our study highlights that significant conductance contrast is possible on a nano-second timescale, which should spur future experimental efforts with a high time resolution. The presence of electrodes could alter the structural dynamics of a single-molecule by reducing the conformational fluctuations, resulting in a smaller ensemble of molecular configurations. Since this study is focused on unraveling the structural changes in single-molecule conductance, we considered a wide range of configurations. Incorporating electrode effects at variety of inter-electrode separation could offer additional insights into the conductance stochasticity of single molecules and should be undertaken in future studies.

Although our findings reveal the dramatic conductance fluctuations between folded and unfolded states, they also highlight the potential to achieve two distinct conductance states through controlled manipulation of ssRNA unfolding and refolding. To this end, state-of-the-art techniques such as optical and magnetic tweezers present promising methods to reversibly switch ssRNA between these two conformational states.[28,29] When combined with a conductance measurement setup, this approach can pave the way for the development of ssRNA-based ultra-scaled memory devices and switches. Additionally, regulating salt concentrations offers a viable strategy to limit conformational fluctuations, ensuring more deterministic performance in applications. We anticipate that the outcomes of this study will inspire future experimental research to harness the high and low conductivity of ssRNA in its folded and unfolded states, thus contributing to the advancement of molecular electronics.

Methods

Molecular dynamics simulation setup

The structures of both ssRNA and dsRNA were created with Nucleic Acid Builder (NAB). The ssRNA sequence is: 5′-GGGGGCGGGG-3′ while the dsRNA sequence is: 5′-GGGGGCGGGG-

Table 2 Energy levels and IPR for lowest and highest conductance conformations for $\Delta P_{\mathrm{dis}} = 15, 20, 25$ Å

	ΔP_{dis}: 15 Å				ΔP_{dis}: 20 Å				ΔP_{dis}: 25 Å			
	Energy (eV)		IPR		Energy (eV)		IPR		Energy (eV)		IPR	
MOs	LCC	HCC	LCC	HCC	LCC	HCC	LCC	HCC	LCC	HCC	LCC	HCC
HOMO	−4.92	−5.00	1.00	**0.74**	−5.03	−5.29	**0.85**	1.00	−5.25	−5.16	1.00	**0.85**
HOMO−1	−5.21	−5.06	0.97	**0.53**	−5.18	−5.31	1.00	**0.72**	−5.28	−5.24	0.68	**0.43**
HOMO−2	−5.30	−5.09	1.00	**0.59**	−5.20	−5.32	1.00	**0.81**	−5.35	−5.29	1.00	**0.65**

LCC: lowest conductance conformation HCC: highest conductance conformation IPR: inverse participation ratio.

3′/3′-CCCCCGCCC-5′. All Molecular Dynamics (MD) simulations were performed in AMBER 20 software with explicit solvent.[30] We have used an RNA OL3 force field with TIP3P for water. Firstly, we perform a two-step minimization on the generated structures. In the first stage, we relax the solvent with counterions by applying a restraint of 50 kcal mol^{-1} force on ssRNA/dsRNA. The minimization step involves 5000 steps with 250 cycles of steepest descent followed by conjugate gradient descent with a non-bonded cutoff of 10 Å. After solvent/counterions are minimized, we perform a similar energy minimization on the whole system. Secondly, the system is heated from 0 to 300 K in a span of 1 ns. The temperature was increased linearly in 5000 steps and then kept constant for the rest of the simulations. For temperature control, we adopted the Langevin thermostat with a 1 ps^{-1} collision frequency. SHAKE algorithm was activated to constrain bonds involving hydrogen atoms with a convergence tolerance of 10^{-5}. Initial velocities were also randomized. During the heating stage, we considered the NVT ensemble (constant volume) with ssRNA/dsRNA restrained with a force of 50 kcal mol^{-1}. Following up, equilibration was performed for 1 ns on the structures and velocities obtained from the previous heating stage. During this step, the target temperature was maintained at 300 K with a Langevin thermostat with 1 ps^{-1} collision frequency but reduced force restraint of 0.5 kcal mol^{-1} on ssRNA/dsRNA to allow structural relaxation. Finally, the production stage was carried out with the final structures and velocities obtained from the equilibration step under the NPT ensemble. For both ssRNA/dsRNA, the production step lasted for 200 ns. Like the previous stages, the SHAKE algorithm and Langevin thermostat were activated. The non-bonded interaction cutoff was set at 10 Å. We have used the Particle Mesh Ewald (PME) method to account for long-range electrostatic interactions.

Molecular dynamics data analysis

To explore the structural stability of ssRNA/dsRNA, we have computed the following metrics based on the MD trajectory: (i) 1D- and 2D-RMSD (ii) end-to-end phosphorus distance (ΔP_{dis}) (iii) hydrogen bonding heatmaps and (iv) backbone dihedral angles. All the MD data analyses were performed with Cpptraj and Pytraj packages.[31] Detailed descriptions of these metrics are as follows:

1D- and 2D-RMSD

Pairwise RMSD of the trajectory was computed with pairwise_rmsd module in Pytraj. 1D-RMSD was derived from the first row of the 2D-RMSD matrix.

End-to-end phosphorus distance (ΔP_{dis})

The distance between phosphorus (P) atoms of the 2nd and 10th residues was calculated using the distance module of Pytraj.

Hydrogen bonding heatmaps

Hydrogen bonding was computed using the *hbond* function of Cpptraj by considering each residue as both a donor mask and an acceptor mask. The hydrogen bonds are detected based on the criteria: angle cutoff of 135° and distance cutoff of 3 Å. The heatmaps were generated from the average number of hydrogen bonds between any two residues and between the base and backbone over a 200 ns trajectory.

Backbone dihedral angles

We extracted the six backbone dihedral angles (α, β, γ, δ, ε, ζ) along with the χ angle. The definitions of these angles are as follows:

$$[\alpha\text{: O3}'(i-1)\text{–P–O5}'\text{–C5}']$$

$$[\beta\text{: P–O5}'\text{–C5}'\text{–C4}']$$

$$[\gamma\text{: O5}'\text{–C5}'\text{–C4}'\text{–C3}']$$

$$[\delta\text{: C5}'\text{–C4}'\text{–C3}'\text{–O3}']$$

$$[\varepsilon\text{: C4}'\text{–C3}'\text{–O3}'\text{–P}(i+1)]$$

$$[\zeta\text{: C3}'\text{–O3}'\text{–P}(i+1)\text{–O5}'(i+1)]$$

$$[\chi\text{ for pyrimidines: O4}'\text{–C1}'\text{–N1–C2}]$$

$$[\chi\text{ for purines: O4}'\text{–C1}'\text{–N9–C4}]$$

where, (i + 1) and (i − 1) represent the next and previous residues.

Additionally, in salt concentration analysis, we have used the *rdf* module of Pytraj to compute the radial distribution function with a bin size of 0.01 Å.

Frame selection procedure

ssRNA. We derived 100 000 conformations (frames) from the MD simulations of ssRNA. Frame selection from this vast dataset involved a two-step process. Firstly, we classify all conformations into multiple categories based on end-to-end phosphorus distance (ΔP_{dis}), a parameter that reflects the proximity of the terminal bases and, by extension, the folding or unfolding state of the conformation. To capture the full spectrum of ssRNA conformational states, we have considered five categories of ΔP_{dis}. However, each category contained hundreds of conformation which makes it computationally expensive to perform DFT/transport calculations on each of them. Hence, in the second step, we refined our frame selection by considering the number of stacked bases so that the impact of base positioning is accounted for in the charge transport. Following the definition in S. Chandra *et al.*,[21] the bases are considered to be stacked when they satisfy the three following conditions: (i) $|z_{jk}| > 2$ (ii) $\rho_{jk} < 2.5$ Å and (iii) $|\alpha_{kj}| < 40°$, where $\rho_{jk} = \sqrt{x_{jk}^2 + y_{jk}^2}$ and (x_{jk}, y_{jk}, z_{jk}) are distances between the center of masses of the two bases (j,k) along the x-, y-, and z-axis. α_{kj} is the angle between normal vectors of bases (j,k). In each category, we classified the conformations into sub-categories based on number of stacked bases, which typically range from 2 to 7. From each of these sub-categories with the same number of stacked bases and almost similar ΔP_{dis}, conformations were sorted based on the sum of all angles ($\Sigma\alpha$) between normal vectors of adjacent bases (α). A set of five frames per sub-category, representative of minimum, maximum, median, 1st, and 3rd quartile values of the sum of angles ($\Sigma\alpha$), was chosen. This yielded a total of 125 conformations.

dsRNA. The abovementioned frame selection procedure is not required for dsRNA as it exhibits significantly greater stability with minimal variation in ΔP_{dis}. Thus, we have performed clustering with VMD software[32] and chosen the head of the cluster for the top five clusters, which accounts for >95% of the population.

It is to be noted that all the selected conformations of both ssRNA and dsRNA undergo a two-step energy minimization process in AMBER 20 before charge transport calculations are performed. In the first step, the solvent and counterions are minimized over 2500 steps with restraint on ssRNA/dsRNA, while during the second step, the whole system undergoes energy minimization for 2500 steps. These energy-minimized structures are used for DFT/transport calculations.

Ab initio DFT modeling

Density functional theory (DFT) calculations have been performed in the Gaussian 16 software package with Gaussian-type orbitals.[33] The hybrid functional B3LYP with a 6-31G** basis set has been used. To incorporate the solvent effect (water in this case), we have included the polarizable continuum model (PCM). For all self-consistent field (SCF) calculations, the default ''tight'' convergence criteria of Gaussian were used. Following this, the Fock (F) and overlap (S) matrices were extracted using *readmat* utility.

To operate with an orthogonal atomic basis set, the Hamiltonian (H) of the system was generated from Fock (F) and overlap (S) matrices by performing Lowdin transformation as follows:

$$H = S^{-\frac{1}{2}} F S^{-\frac{1}{2}} \tag{1}$$

The diagonal terms in H represent the onsite energies of the orbitals, while off-diagonal terms correspond to the hopping energy between orbitals. For the transport calculations, we chose to partition the whole Hamiltonian based on individual bases.

In this approach, the Hamiltonian was rearranged in the following way to obtain a modified Hamiltonian (H_{I}):

$$H_I = \begin{pmatrix} H_{1,1} & H_{1,2} & \cdots & H_{1,9} & H_{1,10} \\ H_{2,1} & H_{2,2} & \cdots & H_{2,9} & H_{2,10} \\ \vdots & \vdots & \ddots & \vdots & \vdots \\ H_{9,1} & H_{9,2} & \cdots & H_{9,9} & H_{9,10} \\ H_{10,1} & H_{10,2} & \cdots & H_{10,9} & H_{10,10} \end{pmatrix} \tag{2}$$

where, $H_{I_{k,k}}$ $k \in [1,10]$ represents the sub-Hamiltonian matrix corresponding to base k. The diagonal/off-diagonal elements within $H_{I_{k,k}}$ describe the onsite potentials of all atomic orbitals in base k and hopping energy between those orbitals respectively. The off-diagonal blocks $H_{I_{k,k'}}$ (where $k \neq k'$; $k, k' \in [1,10]$) indicate the hopping energies between orbitals in base k and k'. The dimension of $H_{I_{k,k}}$ is $\sum_{j=1}^{N_k} b_j$, where b_j is the total number of basis sets used to represent atom j in base k and N_k is the total number of atoms in base k.

Next, a unitary transformation was applied to H_I to obtain the final Hamiltonian (H_{DNA}), which was used in the transport calculation. The transformation is expressed as follows:

$$H_{\text{DNA}} = U^{\dagger} H_I U \tag{3}$$

The unitary matrix U is defined as:

$$U = \begin{pmatrix} u_1 & 0 & \cdots & 0 & 0 \\ 0 & u_2 & \cdots & 0 & 0 \\ \vdots & \vdots & \ddots & \vdots & \vdots \\ 0 & 0 & \cdots & u_9 & 0 \\ 0 & 0 & \cdots & 0 & u_{10} \end{pmatrix} \tag{4}$$

where u_k is a diagonal sub-matrix containing the eigenvectors of $H_{I_{k,k}}$.

Transport calculations

For charge transport calculations, firstly, we compute the retarded Green's function (G^{r}) including self-energies of contacts and decoherence probes as follows:

$$[E - H_{\text{DNA}} - \Sigma_{\text{L}} - \Sigma_{\text{R}} - \Sigma_{\text{B}}(E)]G^{\text{r}} = I \tag{5}$$

where E is the energy, $\Sigma_{\text{L(R)}}$ $\left(\Sigma_{\text{L(R)}} = -\frac{\text{i}\Gamma_{\text{L(R)}}}{2}\right)$ are the self-energies due to left (right) contacts while $\Gamma_{\text{L(R)}}$ represent the corresponding coupling between DNA and left (right) contacts. Σ_{B} depicts combined self-energies of decoherence probes.

In our study, we have considered energy-dependent decoherence probes which is an improvement over the energy-independent model as shown in our previous study.[34] For an energy-dependent decoherence probe, the imaginary part of Σ_{B} is expressed as:

$$\text{Im}[\Sigma_{\text{B}}(E)] = -\frac{\Gamma_{m,k}(E)}{2} = -\left(\Gamma_{\text{B}} \times \exp\left[-\frac{|E - \varepsilon_{m,k}|}{\lambda}\right]\right) \tag{6}$$

where $\Gamma_{\text{k,m}}$ represents the coupling between the decoherence probe and molecular orbital m in base k. Regarding left/right contact self-energies, we have considered the wide-band limit in which $\text{Re}(\Sigma_{\text{L(R)}}) = 0$ and $\text{Im}(\Sigma_{\text{L(R)}})$ = constant.

For all our calculations, we have chosen the following values of parameters: $\Gamma_{\text{L}} = \Gamma_{\text{R}} = 0.1$ eV; $\Gamma_{\text{B}} = 0.1$ eV; $\lambda = 0.1$ eV. All atoms in bases 1 and 10 are connected to left and right contact respectively. The effective transmission is expressed as:

$$T_{\text{eff}} = T_{\text{LR}} + \sum_{k=1}^{N_{\text{b}}} \sum_{l=1}^{N_{\text{b}}} T_{Lk} W_{kl}^{-1} T_{l\text{R}} \tag{7}$$

where T_{LR} represents the coherent transmission between the left and right electrodes. The second term accounts for the contribution to transmission *via* the decoherence probes. The transmission function between probes k and l is given by $T_{kl} = \Gamma_k G^{\mathrm{r}} \Gamma_l G^{\mathrm{a}}$ ($k \in [1,N_{\mathrm{b}}]$), where $G^{\mathrm{a}} = (G^{\mathrm{r}})^{\dagger}$ is the advanced Green's function. The term W_{kl}^{-1} is the inverse of $W_{ij} = (1 - R_{kk})\delta_{kl} - T_{kl}(1 - \delta_{kl})$, where R_{kk} is the reflection probability at probe k, calculated as: $R_{kk} = 1 - \sum_{k \neq l}^{N} T_{kl}$, described in more detail in.[35–38]

Linear response conductance

The zero-bias or linear response conductance is computed from the effective transmission using the following equation:

$$G(E_{\mathrm{F}}) = \frac{2q^2}{h}\int T_{\mathrm{eff}}(E)\frac{\partial f(E)}{\partial E}\mathrm{d}E \tag{8}$$

where $f(E) = \left(1 + \exp\left(\frac{E - E_{\mathrm{f}}}{kT}\right)\right)^{-1}$ is the Fermi distribution. Conductance is calculated with the Fermi energy at the HOMO energy.

Density of states calculation

The density of states calculation involves no contact self-energies. We have considered a very small broadening (η = 0.001). Like transport calculations, we start with computing retarded Green's Function:

$$[(E + \mathrm{i}\eta) - H_{\mathrm{DNA}}]G^{\mathrm{r}} = I \tag{9}$$

The local density of states (LDOS) at an energy point is calculated by solving the following equation:

$$\mathrm{DOS}(i,E) = -\frac{1}{\pi}\mathrm{Im}(G^{\mathrm{r}}(i,i,E)) \tag{10}$$

Wavefunction projection

To compute the probability $|\Psi|^2$ of finding an electron on each base at any energy level, we have computed the projected wavefunction of that energy on each base.[39] We first solve the following eigenvalue problem with Fock (F) and overlap (S) matrices:

$$F\Psi = SE\Psi \tag{11}$$

where E is a diagonal matrix of eigenvalues corresponding to allowed energy levels in the system and Ψ is the eigenvector, the mth column of which corresponds to mth molecular orbitals. The dimension of Ψ is the same as that of the Fock matrix (F).

To find the contribution of each base, we divide the whole system into base-wise fragments. Set of all wavefunctions pertaining to orbitals in a fragment is represented by Ψ_k ($k \in [1,10]$). The contribution of kth base is computed as follows:

$$\Psi_k^{\dagger} S_{k,k} \Psi_k + \sum_{k' \neq k} \Psi_k^{\dagger} S_{k,k'} \Psi_{k'} \tag{12}$$

where, $S_{k,k'}$ represents the sub-matrix in the overlap matrix which corresponds to orbitals in base k and k'. The first component represents the contribution due to the orbitals in the same fragment while the last second component corresponds to overlap with other fragments.

Probable pathways calculation

Parameter definition. To determine the most probable pathways for electron transport in ssRNA, we developed a methodology built upon four key components: (i) inter-base distance, (ii) overlap strength between bases, (iii) available density of states along a path, and (iv) number of bases involved in the pathway. These parameters were computed for all conformations as follows:

(i) Inter-base distance: First, the center of mass of each base was calculated using only the atoms in the nitrogenous base, excluding those in the sugar or backbone. A 2D distance matrix, D, was then constructed, with the distances between the center of masses of all bases.

(ii) Overlap strength: Using the overlap matrix, S, obtained from DFT calculation, we extracted the submatrix $S_{k,k'}$ corresponding to the overlap between any two bases (k,k'). We then calculated the Frobenius norm of the matrix as:

$$\left\|S_{k,k'}\right\|_{\mathrm{F}} = \sqrt{\sum_{p=1}^{N_k}\sum_{q=1}^{N_{k'}}\left|S_{k,k'}(p,q)\right|^2} \tag{13}$$

where N_k and $N_{k'}$ are the number of atomic orbitals in bases k and k' respectively. A 2D overlap strength matrix S_{F} was then generated by applying the Frobenius norm to the overlaps between every pair of bases.

(iii) Available density of states: Partial density of states (PDOS) at kth base for an energy level E was calculated as:

$$\mathrm{PDOS}(k,E) = \sum_{i=1}^{N_k}\mathrm{DOS}(i,E) \tag{14}$$

where N_k is the number of orbitals in base k.

Path generation. We employed a 10-node graph-based methodology, each node of the graph corresponding to a base of the ssRNA. The edges are weighed according to the inter-base distance from the distance matrix D. We then computed all possible simple paths (non-repeating nodes) with the *networkx* package.[40] Note that we computed more than 100 000 paths for each conformation.

Cost calculation. The total cost of any path has two main components, aggregate cost of nodes along the path and aggregate cost of edges along the path. Among the four charge transport parameters indicated above, partial DOS is an attribute of each base (node in the graph), while both inter-base distance and overlap strength relate to pairs of bases (edges in the graph). Therefore, the aggregate node cost along a path is based on the sum of partial DOS of all bases involved in the path and the aggregate edge cost is based on the distance matrix D and the overlap strength matrix S_{F}. The path length is used as a scaling factor for both node and edge costs. The final expressions for computing the aggregate node cost, aggregate edge cost, and path cost (''score'') are as follows:

Aggregate node cost

$$\mathrm{Nc} = \frac{L}{\sum_{k=1}^{L} \mathrm{PDOS}\big(n_{\mathrm{p}}(k), E\big)} \tag{15}$$

Aggregate edge cost

$$\mathrm{Ec} = (L-1) \times \frac{\sum_{k=1}^{L-1} D\big(n_{\mathrm{p}}(k), n_{\mathrm{p}}(k+1)\big)}{\sum_{k=1}^{L-1} S_{\mathrm{F}}\big(n_{\mathrm{p}}(k), n_{\mathrm{p}}(k+1)\big)} \tag{16}$$

Path cost

$$\mathrm{Score} = \mathrm{Nc} + \mathrm{Ec} \tag{17}$$

where L is the length of the path (total number of nodes in a path), $n_{\mathrm{p}}(k)$ is the kth node in a path starting and ending at bases 1 and 10 (terminal bases) respectively, and E is the energy level.

Author contributions

M. P. A. conceptualized the research problem. A. D. refined this as the work progressed. A. D. is responsible for data curation. Formal analysis of transport results was performed by A. D. and M. P. A. Formal analysis of data analysis was performed primarily by A. D. and A. K. D. with M. P. A. contributing. The methodology of transport properties was designed by M. P. A., MD was designed by A. D. and M. P. A., and the work on optimum transport path was designed by A. D. and A. K. D. All calculations were performed by A. D. The first draft was written by A. D. A. K. D. and M. P. A. extensively rewrote parts of the manuscript. The code used for transport was already available in M. P. A's group. A. D. wrote the code to determine the optimum transport path. A. D. performed the work required for visualization with input from A. K. D. and M. P. A. M. P. A. was responsible for funding acquisition. M. P. A. supervised the research work and was responsible for project administration.

Conflicts of interest

The authors declare no competing interests.

Data availability

All data are provided in this manuscript and ESI.†

Acknowledgements

We acknowledge the support of the National Science Foundation grants GCR-2317843, FuSe-2235294 and FMRG-2328217. We also acknowledge the HYAK supercomputing facility at the University of Washington. MPA thanks Prof. Juan M Artés Vivancos (UMass) for insightful discussion on single molecule experiments. The AI tool Grammarly has been used in the process of writing this manuscript.

References

1 M. J. Moore, From Birth to Death: The Complex Lives of Eukaryotic mRNAs, *Science*, 2005, **309**, 1514–1518.

2 J. L. Rinn and H. Y. Chang, Genome Regulation by Long Noncoding RNAs, *Annu. Rev. Biochem.*, 2012, **81**, 145–166.

3 P. Nissen, J. Hansen, N. Ban, P. B. Moore and T. A. Steitz, The Structural Basis of Ribosome Activity in Peptide Bond Synthesis, *Science*, 2000, **289**, 920–930.

4 T. H. D. Nguyen, *et al.*, The architecture of the spliceosomal U4/U6.U5 tri-snRNP, *Nature*, 2015, **523**, 47–52.

5 H. F. Noller, V. Hoffarth and L. Zimniak, Unusual Resistance of Peptidyl Transferase to Protein Extraction Procedures, *Science*, 1992, **256**, 1416–1419.

6 R. Giegé, M. Frugier and J. Rudinger, tRNA mimics, *Curr. Opin. Struct. Biol.*, 1998, **8**, 286–293.

7 J. E. G. McCarthy and C. Gualerzi, Translational control of prokaryotic gene expression, *Trends Genet.*, 1990, **6**, 78–85.

8 M. Chamorro, N. Parkin and H. E. Varmus, An RNA pseudoknot and an optimal heptameric shift site are required for highly efficient ribosomal frameshifting on a retroviral messenger RNA, *Proc. Natl. Acad. Sci. U. S. A.*, 1992, **89**, 713–717.

9 J. Zhang, Y. Fei, L. Sun and Q. C. Zhang, Advances and opportunities in RNA structure experimental determination and computational modeling, *Nat. Methods*, 2022, **19**, 1193–1207.

10 M. G. Seetin and D. H. Mathews, RNA Structure Prediction: An Overview of Methods, in *Bacterial Regulatory RNA: Methods and Protocols*, ed. K. C. Keiler, Humana Press, Totowa, NJ, 2012, pp. 99–122, DOI: 10.1007/978-1-61779-949-5_8.

11 P. P. Gardner and R. Giegerich, A comprehensive comparison of comparative RNA structure prediction approaches, *BMC Bioinf.*, 2004, **5**, 140.

12 E. K. S. McRae, *et al.*, Structure, folding and flexibility of co-transcriptional RNA origami, *Nat. Nanotechnol.*, 2023, **18**, 808–817.

13 H. C. Høiberg, S. M. Sparvath, V. L. Andersen, J. Kjems and E. S. Andersen, An RNA Origami Octahedron with Intrinsic siRNAs for Potent Gene Knockdown, *Biotechnol. J.*, 2019, **14**, 1700634.

14 A. Krissanaprasit, *et al.*, Genetically Encoded, Functional Single-Strand RNA Origami: Anticoagulant, *Adv. Mater.*, 2019, **31**, 1808262.

15 M. T. A. Nguyen, G. Pothoulakis and E. S. Andersen, Synthetic Translational Regulation by Protein-Binding RNA Origami Scaffolds, *ACS Synth. Biol.*, 2022, **11**, 1710–1718.

16 D. Han, *et al.*, Single-stranded DNA and RNA origami, *Science*, 2017, **358**, eaao2648.

17 N. S. Vallina, E. K. S. McRae, C. Geary and E. S. Andersen, An RNA origami robot that traps and releases a fluorescent aptamer, *Sci. Adv.*, 2024, **10**, eadk1250.

18 Y. Li, *et al.*, Comparing Charge Transport in Oligonucleotides: RNA:DNA Hybrids and DNA Duplexes, *J. Phys. Chem. Lett.*, 2016, **7**, 1888–1894.

19 Y. Li, J. M. Artés and J. Hihath, Long-Range Charge Transport in Adenine-Stacked RNA:DNA Hybrids, *Small*, 2016, **12**, 432–437.

20 S. Chandra, *et al.*, Single-molecule conductance of double-stranded RNA oligonucleotides, *Nanoscale*, 2022, **14**, 2572–2577.

21 S. Chandra, *et al.*, Charge transport in individual short base stacked single-stranded RNA molecules, *Sci. Rep.*, 2023, **13**, 19858.

22 M. Gonçalves, B. Amorim, F. Riche, E. V. Castro and P. Ribeiro, Incommensurability enabled quasi-fractal order in 1D narrow-band moiré systems, *Nat. Phys.*, 2024, **20**, 1933–1940.

23 A. Henning-Knechtel, D. Thirumalai and S. Kirmizialtin, Differences in ion-RNA binding modes due to charge density variations explain the stability of RNA in monovalent salts, *Sci. Adv.*, 2022, **8**, eabo1190.

24 J. F. Hopkins, S. Panja, S. A. N. McNeil and S. A. Woodson, Effect of salt and RNA structure on annealing and strand displacement by Hfq, *Nucleic Acids Res.*, 2009, **37**, 6205–6213.

25 J. J. McDermott, B. Civic and A. Barkan, Effects of RNA structure and salt concentration on the affinity and kinetics of interactions between pentatricopeptide repeat proteins and their RNA ligands, *PLoS One*, 2018, **13**, e0209713.

26 Y.-L. Chen and L. Pollack, Salt Dependence of A-Form RNA Duplexes: Structures and Implications, *J. Phys. Chem. B*, 2019, **123**, 9773–9785.

27 S. K. Kolev, P. St. Petkov, T. I. Milenov and G. N. Vayssilov, Sodium and Magnesium Ion Location at the Backbone and at the Nucleobase of RNA: Ab Initio Molecular Dynamics in Water Solution, *ACS Omega*, 2022, **7**, 23234–23244.

28 C. J. Bustamante, Y. R. Chemla, S. Liu and M. D. Wang, Optical tweezers in single-molecule biophysics, *Nat. Rev. Methods Primers*, 2021, **1**, 1–29.

29 R. Tapia-Rojo, M. Mora and S. Garcia-Manyes, Single-molecule magnetic tweezers to probe the equilibrium dynamics of individual proteins at physiologically relevant forces and timescales, *Nat. Protoc.*, 2024, **19**, 1779–1806.

30 D. A. Case, *et al.*, AmberTools, *J. Chem. Inf. Model.*, 2023, **63**, 6183–6191.

31 D. R. Roe and T. E. I. Cheatham, PTRAJ and CPPTRAJ: Software for Processing and Analysis of Molecular Dynamics Trajectory Data, *J. Chem. Theory Comput.*, 2013, **9**, 3084–3095.

32 W. Humphrey, A. Dalke and K. Schulten, VMD: Visual molecular dynamics, *J. Mol. Graphics*, 1996, **14**, 33–38.

33 M. J. Frisch, G. W. Trucks, H. B. Schlegel, G. E. Scuseria, M. A. Robb, J. R. Cheeseman, G. Scalmani, V. Barone, G. A. Petersson, H. Nakatsuji, X. Li, M. Caricato, A. V. Marenich, J. Bloino, B. G. Janesko, R. Gomperts, B. Mennucci, H. P. Hratchian, J. V. Ortiz, A. F. Izmaylov, J. L. Sonnenberg, D. Williams-Young, F. Ding, F. Lipparini, F. Egidi, J. Goings, B. Peng, A. Petrone, T. Henderson, D. Ranasinghe, V. G. Zakrzewski, J. Gao, N. Rega, G. Zheng, W. Liang, M. Hada, M. Ehara, K. Toyota, R. Fukuda, J. Hasegawa, M. Ishida, T. Nakajima, Y. Honda, O. Kitao, H. Nakai, T. Vreven, K. Throssell, J. A. Montgomery, Jr., J. E. Peralta, F. Ogliaro, M. J. Bearpark, J. J. Heyd, E. N. Brothers, K. N. Kudin, V. N. Staroverov, T. A. Keith, R. Kobayashi, J. Normand, K. Raghavachari, A. P. Rendell, J. C. Burant, S. S. Iyengar, J. Tomasi, M. Cossi, J. M. Millam, M. Klene, C. Adamo, R. Cammi, J. W. Ochterski, R. L. Martin, K. Morokuma, O. Farkas, J. B. Foresman and D. J. Fox, *Gaussian 16*, 2016.

34 H. Mohammad and M. P. Anantram, Charge transport through DNA with energy-dependent decoherence, *Phys. Rev. E*, 2023, **108**, 044403.

35 A. De, H. Mohammad and Y. Wang, *et al.*, Performance analysis of DNA crossbar arrays for high-density memory storage applications, *Sci. Rep.*, 2023, DOI: **10.1038/s41598-023-33004-6**.

36 A. De *et al.*, Modeling and Simulation of DNA Origami based Electronic Read-only Memory. in 2022 IEEE 22nd International Conference on Nanotechnology (NANO) 385–388, 2022, DOI: **10.1109/NANO54668.2022.9928676**.

37 H. Mohammad, *et al.*, Role of intercalation in the electrical properties of nucleic acids for use in molecular electronics, *Nanoscale Horiz.*, 2021, **6**, 651–660.

38 S. R. Patil, *et al.*, Quantum Transport in DNA Heterostructures: Implications for Nanoelectronics, *ACS Appl. Nano Mater.*, 2021, **4**, 10029–10037.

39 J. M. Artés, Y. Li, J. Qi, M. P. Anantram and J. Hihath, Conformational gating of DNA conductance, *Nat. Commun.*, 2015, **6**, 8870.

40 Exploring Network Structure, Dynamics, and Function using NetworkX – SciPy Proceedings. **https://proceedings.scipy.org/articles/TCWV9851** (2008).